

## RESEARCH OUTPUTS / RÉSULTATS DE RECHERCHE

### Hierarchical Zeolite Single-Crystal Reactor for Excellent Catalytic Efficiency

Sun, Ming Hui; Zhou, Jian; Hu, Zhi Yi; Chen, Li Hua; Li, Li Yuan; Wang, Yang Dong; Xie, Zai Ku; Turner, Stuart; Van Tendeloo, Gustaaf; Hasan, Tawfique; Su, Bao Lian

*Published in:*  
Matter

*DOI:*  
[10.1016/j.matt.2020.07.016](https://doi.org/10.1016/j.matt.2020.07.016)

*Publication date:*  
2020

*Document Version*  
Version created as part of publication process; publisher's layout; not normally made publicly available

[Link to publication](#)

*Citation for published version (HARVARD):*  
Sun, MH, Zhou, J, Hu, ZY, Chen, LH, Li, LY, Wang, YD, Xie, ZK, Turner, S, Van Tendeloo, G, Hasan, T & Su, BL 2020, 'Hierarchical Zeolite Single-Crystal Reactor for Excellent Catalytic Efficiency', *Matter*, vol. 3, no. 4, pp. 1226-1245. <https://doi.org/10.1016/j.matt.2020.07.016>

#### General rights

Copyright and moral rights for the publications made accessible in the public portal are retained by the authors and/or other copyright owners and it is a condition of accessing publications that users recognise and abide by the legal requirements associated with these rights.

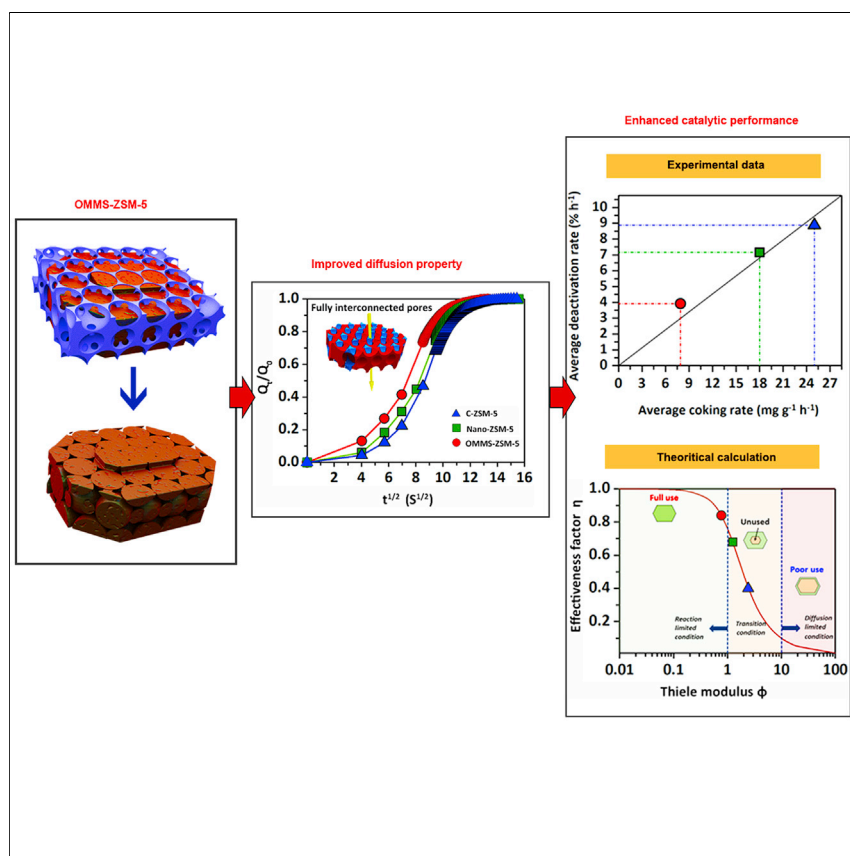
- Users may download and print one copy of any publication from the public portal for the purpose of private study or research.
- You may not further distribute the material or use it for any profit-making activity or commercial gain
- You may freely distribute the URL identifying the publication in the public portal ?

#### Take down policy

If you believe that this document breaches copyright please contact us providing details, and we will remove access to the work immediately and investigate your claim.

## Article

## Hierarchical Zeolite Single-Crystal Reactor for Excellent Catalytic Efficiency



Zeolite single crystal with a fully interconnected, highly ordered, and tunable intracrystalline macro-/meso-/microporous hierarchy has been synthesized by a versatile confined zeolite crystallization process for the first time. These zeolite single-crystal reactors show unprecedentedly high diffusion efficiency and excellent catalytic performance. The synthesis route is quite versatile and has been extended to synthesize single crystals with any kind of chemical compositions. The successful synthesis of such single crystals will open a large panel of applications in different areas.

Ming-Hui Sun, Jian Zhou, Zhi-Yi Hu, ..., Gustaaf Van Tendeloo, Tawfique Hasan, Bao-Lian Su

chenlihua@whut.edu.cn (L.-H.C.)  
 xzk@sinopec.com (Z.-K.X.)  
 staf.vantendeloo@unantwerpen.be (G.V.T.)  
 bao-lian.su@unamur.be (B.-L.S.)

## HIGHLIGHTS

Hierarchically porous zeolite single-crystal reactors have been demonstrated

These crystals have a fully interconnected and highly ordered multimodal porosity

Zeolite single-crystal reactors show excellent catalytic efficiency and activity

The confined crystallization process is a quite simple and versatile strategy



## Demonstrate

Proof-of-concept of performance with intended application/response

Sun et al., Matter 3, 1–20  
 October 7, 2020 © 2020 Elsevier Inc.  
<https://doi.org/10.1016/j.matt.2020.07.016>

Article

# Hierarchical Zeolite Single-Crystal Reactor for Excellent Catalytic Efficiency

Ming-Hui Sun,<sup>1,2,8</sup> Jian Zhou,<sup>3,8</sup> Zhi-Yi Hu,<sup>1,4,5,8</sup> Li-Hua Chen,<sup>1,\*</sup> Li-Yuan Li,<sup>3</sup> Yang-Dong Wang,<sup>3</sup> Zai-Ku Xie,<sup>3,\*</sup> Stuart Turner,<sup>5</sup> Gustaaf Van Tendeloo,<sup>4,5,\*</sup> Tawfique Hasan,<sup>6</sup> and Bao-Lian Su<sup>1,2,7,9,\*</sup>

## SUMMARY

As a size- and shape-selective catalyst, zeolites are widely used in petroleum and fine-chemicals processing. However, their small micropores severely hinder molecular diffusion and are sensitive to coke formation. Hierarchically porous zeolite single crystals with fully interconnected, ordered, and tunable multimodal porosity at macro-, meso-, and microlength scale, like in leaves, offer the ideal solution. However, their synthesis remains highly challenging. Here, we report a versatile confined zeolite crystallization process to achieve these superior properties. Such zeolite single crystals lead to significantly improved mass transport properties by shortening the diffusion length while maintaining shape-selective properties, endowing them with a high efficiency of zeolite crystals, enhanced catalytic activities and lifetime, highly reduced coke formation, and reduced deactivation rate in bulky-molecule reactions and methanol-to-olefins process. Their industrial utilization can lead to the design of innovative and intensified reactors and processes with highly enhanced efficiency and minimum energy consumption.

## INTRODUCTION

Zeolites are one of the most important catalytic materials used today. Each zeolite crystal can be considered as a catalytic reactor.<sup>1–4</sup> However, the slow transport of the reactants and products within their intracrystalline small microporous channels greatly hinders their efficiency in catalysis and separation. It is highly desirable to reduce the diffusion limitations within each zeolite crystal.<sup>5</sup> The introduction of additional interconnected intracrystalline hierarchical mesopores or/and macropores is thus an efficient strategy toward this goal.<sup>6–11</sup> In comparison with conventional dealumination methods, which are based on random removal of Al or Si atoms from zeolite frameworks through acid or alkali leaching<sup>12–14</sup> or chemical treatment,<sup>15</sup> templating methods<sup>16–28</sup> allow precise control of the density and the size of additional mesopores or macropores, generate much fewer defects in the zeolite framework, and can avoid any negative impact on crystallinity and active sites of the zeolite crystals. Tsapatsis et al. realized the synthesis of size-tunable zeolite nanocrystals (MFI,<sup>17–19</sup> BEA,<sup>20</sup> and FAU<sup>20</sup>) with various intercrystalline mesoporosities using mesoporous carbon templates by steam-assisted crystallization<sup>17–19</sup> or hydrothermal synthesis<sup>20</sup> for improved catalytic performance in ethanol dehydration.<sup>19</sup> However, the synthesis of zeolite single crystals with intracrystalline hierarchically porous structure still remains a great challenge. Schwieger et al. elegantly synthesized microporous MFI-type (Silicalite-1,<sup>21</sup> ZSM-5,<sup>22,23</sup> and TS-1<sup>24</sup>) zeolite single crystals by steam-assisted crystallization of mesoporous silica spheres. The embedded

## Progress and Potential

Zeolite single crystal with a fully interconnected, highly ordered, and tunable intracrystalline macro-/meso-/microporous hierarchy has been synthesized. Such a unique single-crystalline hierarchical structure has never been reported. Unprecedentedly high diffusion efficiency within each of zeolite single crystals is achieved. This is of crucial importance for catalytic and separation processes in terms of their performance and energy and raw materials consumption. These zeolite single crystals show excellent catalytic performance. The synthesis route has been extended to the synthesis of any kind of zeolite structures and zeotype materials, including Beta, TS-1, Y, and SAPO-34, for a large series of catalytic reactions. Most importantly, this strategy is versatile and can be used to synthesize single crystals of solids of any chemical compositions. The successful synthesis of such single crystals will open a large panel of applications of these materials in different areas.

intracrystalline macropores in ZSM-5 zeolite and TS-1 zeolite can significantly improve the catalyst performance in the methanol-to-olefins (MTO) reaction<sup>22,23</sup> and the liquid-phase epoxidation of 2-octene.<sup>24</sup>

The interconnectivity between the intrinsic microporosity of zeolites and additional meso- or/and macroporosity is essential to improve their mass transport properties.<sup>5</sup> This leads to a better accessibility to the active sites located within the micropore system of the zeolites.<sup>29</sup> Many advanced techniques have been developed to probe the interconnectivity of the pores.<sup>30</sup> Pérez-Ramírez et al. contributed greatly to obtaining insight into the interconnectivity of the hierarchical pores,<sup>31</sup> including gas adsorption studies,<sup>32</sup> mercury porosimetry,<sup>33</sup> gravimetric uptake of bulking alkanes,<sup>34</sup> infrared spectroscopy of substituted alkylpyridines with different size,<sup>35</sup> and positron annihilation lifetime spectroscopy.<sup>36,37</sup> In the same way, advanced imaging techniques based on electron tomography and rotation electron diffraction,<sup>21,28</sup> continuous-flow variable-temperature hyperpolarized <sup>129</sup>Xe nuclear magnetic resonance (NMR),<sup>38,39</sup> and pulsed field gradient (PFG) NMR<sup>40,41</sup> have also been proved to be powerful tools for assessing the pore interconnectivity in hierarchically structured zeolites.

More precise control over the location and interconnectivity of the additional porosity could offer potential gains from the structural modification.<sup>42</sup> To address this, Liu et al.<sup>27</sup> designed a cationic amphiphilic copolymer to synthesize ZSM-5 zeolite single-crystalline sheets with abundant and highly interconnected b-axis-aligned mesoporous channels. This approach resulted in much higher catalytic activities for bulky-molecule conversion than bulk ZSM-5 and ZSM-5 with randomly oriented mesopores, although the stability and shape selectivity needed further improvement.<sup>27</sup> Many classes of organisms in both plants and animals contain hierarchical networks of interconnected pores to maximize mass transport and rates of reactions for the highest efficiency and the lowest energy consumption. It is thus highly desirable to construct such hierarchical networks of interconnected pores within each zeolite crystal. However, hierarchically structuring tunable mesoporosity and macroporosity simultaneously with excellent interconnectivity, desired location, and high ordering within each zeolite single crystal to maximize the benefits of the porous hierarchy in catalytic reactions still remains highly challenging.<sup>10,42</sup>

We report the synthesis of ZSM-5 zeolite single crystals with a fully interconnected and highly ordered intracrystalline macro-/meso-/microporous hierarchy in all directions, as occurs in leaves, through a versatile templating strategy via an *in situ* bottom-up confined zeolite crystallization process (Figure 1). The unique hierarchical structure of our single zeolite crystals with high thermal and hydrothermal stability and excellent mechanical strength can maximize the intracrystalline diffusion rate of reactants and products and the accessibility to active sites; for example, the effective diffusion rate of molecules in our zeolite single crystals reaches 10- and 5-fold higher than that of benchmark commercial micro-sized mesoporous ZSM-5 and the state-of-the-art nanosized macroporous ZSM-5, respectively. The efficiency of each of our zeolite single crystals in bulky 1,3,5-triisopropylbenzene (TIPB) cracking reaction can reach a high value of 0.84, which is doubled compared with that of benchmark commercial ZSM-5 catalyst and 20% higher than that of the state-of-the-art nanosized ZSM-5 catalyst. All of these excellent properties lead to a significant reduction in coking and deactivation rate, outstanding catalytic activity and selectivity, and highly improved catalyst lifetime in bulky-molecule reactions and MTO process. The average coking rate in MTO reaction using our zeolite single crystals can reach 8.9- and 7.2-fold lower, and their lifetime can be extended 13-

<sup>1</sup>State Key Laboratory of Advanced Technology for Materials Synthesis and Processing, Wuhan University of Technology, Wuhan 430070, Hubei, China

<sup>2</sup>Laboratory of Inorganic Materials Chemistry (CMI), University of Namur, 5000 Namur, Wallonia, Belgium

<sup>3</sup>State Key Laboratory of Green Chemical Engineering and Industrial Catalysis, Shanghai Research Institute of Petrochemical Technology, SINOPEC, Shanghai 201208, China

<sup>4</sup>Nanostructure Research Centre (NRC), Wuhan University of Technology, Wuhan 430070, Hubei, China

<sup>5</sup>Electron Microscopy for Materials Science (EMAT), University of Antwerp, 2020 Antwerp, Flemish Region, Belgium

<sup>6</sup>Cambridge Graphene Centre, University of Cambridge, Cambridge CB3 0DS, UK

<sup>7</sup>Clare Hall, University of Cambridge, Cambridge CB2 1EW, UK

<sup>8</sup>These authors contributed equally

<sup>9</sup>Lead Contact

\*Correspondence:  
[chenlihua@whut.edu.cn](mailto:chenlihua@whut.edu.cn) (L.-H.C.),  
[xzk@sinopec.com](mailto:xzk@sinopec.com) (Z.-K.X.),  
[staf.vantendeloo@unantwerpen.be](mailto:staf.vantendeloo@unantwerpen.be) (G.V.T.),  
[bao-lian.su@unamur.be](mailto:bao-lian.su@unamur.be) (B.-L.S.)

<https://doi.org/10.1016/j.matt.2020.07.016>

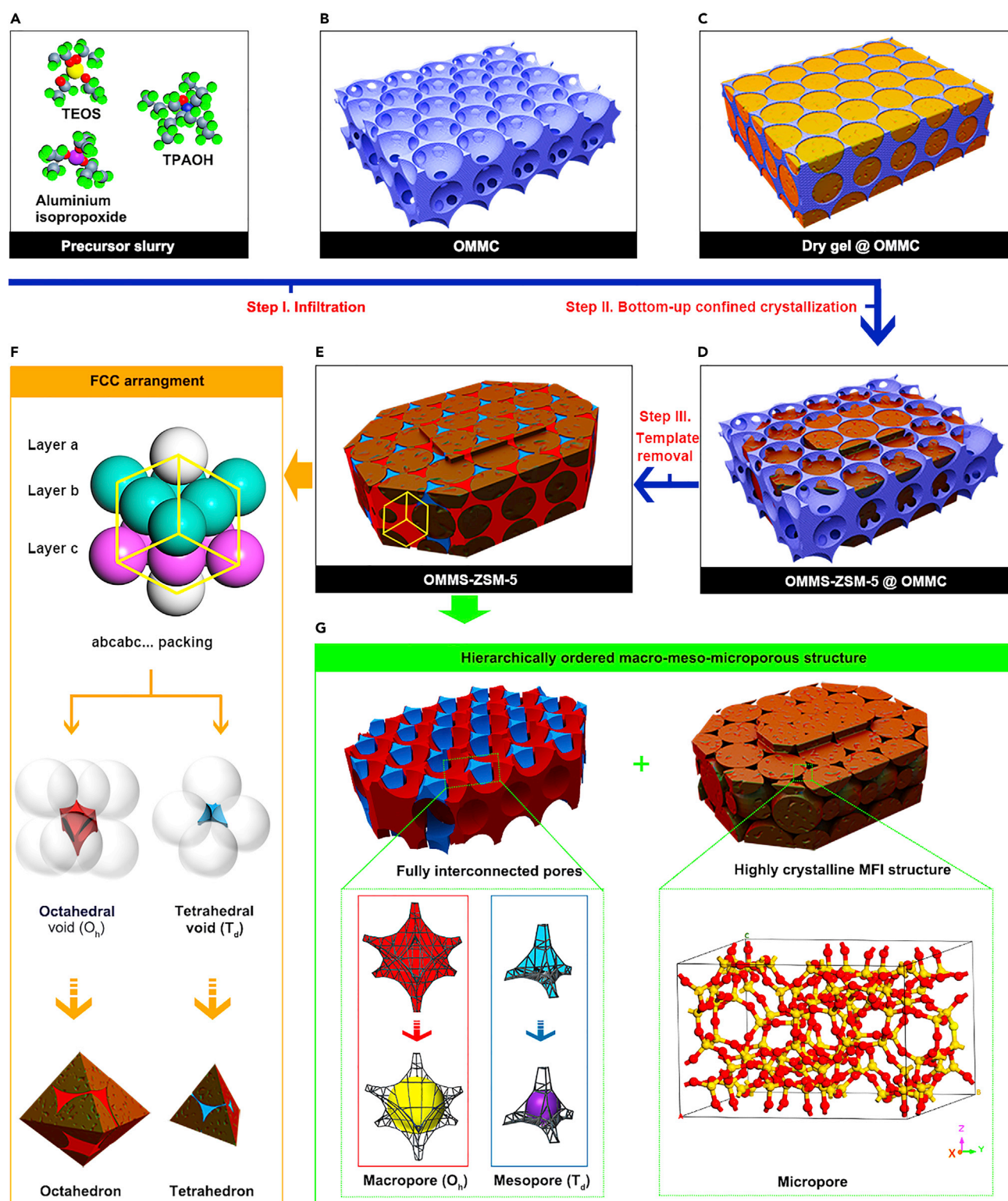


**Figure 1. Synthesis and Structure of OMMS-ZSM-5**

(A–E) Schematic illustration of the synthesis route of OMMS-ZSM-5, from precursor slurry (A) via OMMC (B), dry gel@OMMC (C), OMMS-ZSM-5@OMMC (D), to OMMS-ZSM-5 (E).



**Figure 1. Continued**

(F) The enlarged image of the selected yellow cubic area in (E), confirming the *abcabc...* stacking in FCC arrangement. The units in layer a are shaded white, those in layer b are green, and those in layer c are pink. Such FCC arrangement contains two voids: the tetrahedral void ( $T_d$ , blue) and the octahedral void ( $O_h$ , red).

(G) Schematic illustration of hierarchically ordered macro-meso-microporous structure in OMMS-ZSM-5.

and 3.5-fold longer than that of benchmark commercial micro-sized mesoporous ZSM-5 and state-of-the-art nanosized macroporous ZSM-5, respectively. It is envisioned that the catalytic reactor can be made solely by zeolite single crystals. The excellent performance of zeolite single crystals can be fully exploited in the catalytic reactions without any negative effect of binder and additives and with highly enhanced efficiency, high catalytic activity, selectivity, and lifetime, and minimum energy, time, and raw-material consumption. Most importantly, the upscalable and versatile synthesis strategy has been used to synthesize single crystals of any kind of zeolite structures and zeotype materials and can be extended to fabricate single-crystalline solids of any chemical composition such as transition metal oxides (e.g.,  $\text{TiO}_2$ ,  $\text{ZnO}$ ), phosphate compounds, silicate compounds, and perovskites. These new hierarchically meso-/macroporous materials with single-crystalline nature will open a large panel of applications not only in adsorption, catalysis, and separation, but also in energy storage and conversion, and will create new research areas.

## RESULTS AND DISCUSSION

### Hierarchical Zeolite Single Crystals

Hierarchically ordered macro-/mesoporous carbon (OMMC) (Figures 1B and S1) with an inverse opal structure is used as the meso-/macroporous template.<sup>43,44</sup> The key advantage is that such a template provides a confined and tailorable space for the formation of well-shaped hierarchically porous zeolite single crystals (Figures 1C and 1D). The synthesis of such uniform zeolite single crystals involves three steps: (1) infiltration of zeolite precursor slurry into OMMC template (step 1 in Figure 1), (2) steam-assisted crystallization (SAC) of precursors confined in OMMC template (step 2 in Figure 1), and (3) template removal (step 3 in Figure 1). Each zeolite single crystal is made up of an assembly of tightly interconnected small zeolite spheres in a closely packed face-centered cubic (FCC) arrangement (Figure 1E), which inherits the highly ordered FCC structure of the original polystyrene (PS) opaline crystal structure for the OMMC template fabrication (Figure S2). The FCC arrangement of these tightly interconnected small zeolite spheres results in the formation of tetrahedral ( $T_d$ ) and octahedral ( $O_h$ ) voids by four and six spheres from two layers (Figures 1F and S3–S5; Video S1), respectively. Such periodically arranged  $T_d$  and  $O_h$  voids within one zeolite single crystal, in addition to the intrinsic microporosity of zeolite, provide an ordered, fully interconnected meso- and macroporous structure (Figure 1G; Video S1), precisely replicating the OMMC template (Figure S1).

As proof of concept, hierarchically ordered and highly interconnected macro-/meso-/microporous ZSM-5 single crystals with a tunable Si/Al molar ratio from 30 to  $\infty$  and tunable mesopore and macropore size have been synthesized. We denote the as-synthesized samples as OMMS-ZSM-5(*x*,*y*); OMMS represents ordered macro-/mesoporous zeolite single crystals, whereas *x* and *y* indicate the macropore size (nm) of the OMMC templates and the obtained Si/Al molar ratio, respectively.

Scanning electron microscopy (SEM) images show that after 10 h of crystallization, all the crystals of OMMS-ZSM-5(400,30) used as a representative sample for illustration exhibit a truncated hexagonal prism morphology (Figures 2A–2D). Although the size of the OMMC template is tens of microns, the obtained zeolite single crystals are

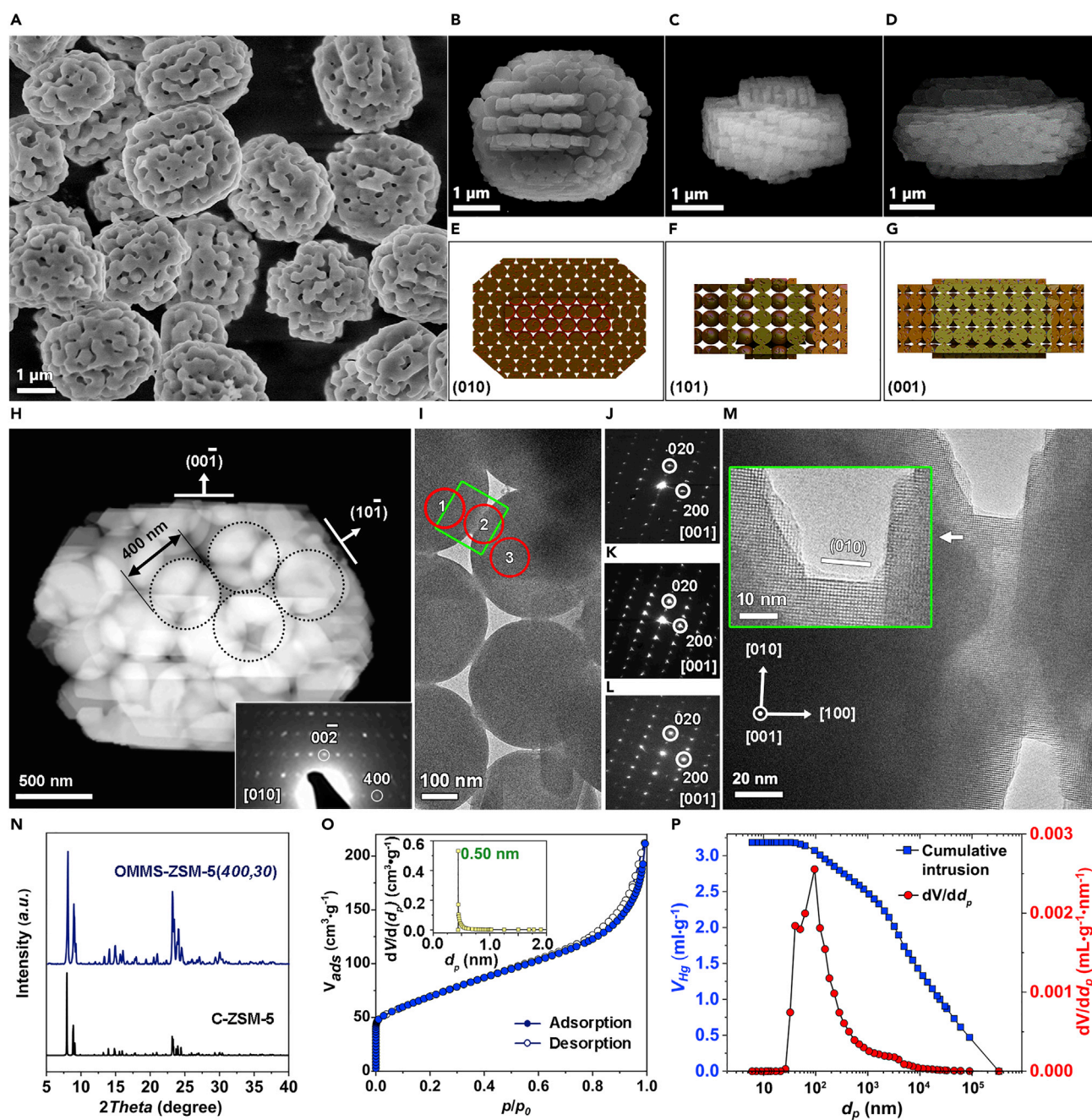


**Figure 2. Characterization of OMMS-ZSM-5**

(A–D) SEM images of OMMS-ZSM-5(400,30).

(E–G) Schematics of an individual crystal from three directions, (010) (E), (101) (F), and (001) (G) corresponding to (B), (C), and (D), respectively.

(H) HAADF-STEM image and ED pattern (inset) of an individual zeolite.

(I) TEM image of enlarged area in (H).

(J–L) SAED patterns of zone 1 (J), zone 2 (K), and zone 3 (L) in (I).

(M) HRTEM images of green area in (I) with enlarged intergrowth region inset.

(N–P) XRD pattern (N), Argon adsorption-desorption isotherms (O), and micropore size distribution (inset) and mercury intrusion (P) of OMMS-ZSM-5(400,30).

well shaped with a similar crystal size of 4–5  $\mu\text{m}$  (Figure 2A). The final size and the uniformity of the zeolite single crystals are highly dependent on the mass ratio of  $\text{SiO}_2$  and OMMC template ( $\text{mSiO}_2/\text{mOMMC}$ ) and the crystallization time (Figures S6 and S7). When the  $\text{mSiO}_2/\text{mOMMC}$  mass ratio is low, the macropores of the OMMC template can only partly be filled by the dry gel and only several zeolite single crystals with different crystal size are obtained (Figure S6), whereas at high  $\text{mSiO}_2/\text{mOMMC}$  ratio all the porosities of the OMMC template can be fully filled by the dry gel and the uniform zeolite single crystals are formed. Upon increasing the crystallization time to 10 h, zeolite single crystals reach their maximum size of 4–5  $\mu\text{m}$  (Figure S7). The highly ordered arrangement of uniformly sized and tightly interconnected small zeolite spheres can be clearly visualized from three different directions in the representative SEM images (Figures 2B–2D) and the corresponding schematic illustrations (Figures 2E–2G) of one individual zeolite crystal. Typical high-angle annular dark field scanning transmission electron microscopy (HAADF-STEM) images reveal that tightly packed and intergrown spheres are imprinted in a highly ordered arrangement within one entire zeolite crystal of OMMS-ZSM-5(400,30), indicating a positive replication of the OMMC template. The diameter of the small zeolite spheres is  $\sim 400$  nm (Figure 2H), identical to the macropore size of the OMMC template and slightly smaller than the size of the PS spheres ( $\sim 420$  nm) used for the OMMC template fabrication (Figure S2). The corresponding selected area electron diffraction (SAED) pattern of one zeolite crystal (Figure 2H, inset) contains discrete diffraction spots and can be indexed according to the MFI-type zeolite along the [010] zone axis, providing the clear evidence of the single-crystalline nature of OMMS-ZSM-5(400,30). By indexing the diffraction pattern, the crystal facets can be readily identified. The largest facets, oriented perpendicular to the electron beam, are (010) type, while the smaller side facets are (101) and (001) type. The dominance of the (010) surface facets can be explained by the MFI-type zeolite crystal preferential growth direction, being in accordance with theoretical calculations predicting the lowest surface energy for the (010) facet.<sup>27</sup> A typical joint between two spheres can be seen in Figure 2I. SAED patterns taken from three different regions of the joint (Figure 2I, zone 1 to zone 3) show that the two spheres, including the half sphere on the left (Figure 2J), the joint area (Figure 2K), and the sphere on the right (Figure 2L), all have the same [001] orientation. This unequivocally confirms the continuous crystalline phase in the same axis. The high-resolution transmission electron microscopy (HRTEM) image (Figure 2M and inset) of the area indicated by the green rectangle in Figure 2I further reveals a continuous, uniform, and dislocation-free lattice arrangement at the joint over the entire image region. No (sub)grain boundaries or interfaces are observed. This proves that all the spheres organized in an FCC arrangement are not independent but crystallized in the same orientation and intergrown to form the entire zeolite single crystal. Besides, no planar defects such as stacking faults, twin formation, or dislocations are observed, confirming the pristine structure throughout the zeolite crystal.

X-ray diffraction (XRD) pattern of OMMS-ZSM-5(400,30) is compared with a standard PDF card (Figure 2N), confirming the formation of a pure MFI zeolite phase with excellent crystallinity. The intrinsic microporosity of zeolite single crystals is determined using Ar adsorption while  $\text{N}_2$  adsorption is adopted to investigate the mesoporosity. OMMS-ZSM-5(400,30) shows type I isotherms with a micropore size distribution centered at 5.3 Å, characteristic of ZSM-5 zeolite with ten-membered ring channels (Figure 2O and inset).<sup>45</sup> The micropore surface area and volume of OMMS-ZSM-5(400,30) are  $299 \text{ m}^2 \text{ g}^{-1}$  and  $0.14 \text{ cm}^3 \text{ g}^{-1}$ , respectively (Table S1), indicating that the formation of a hierarchically macro-/mesoporous system does not influence its inherent microporous structure. The existence of mesopores in



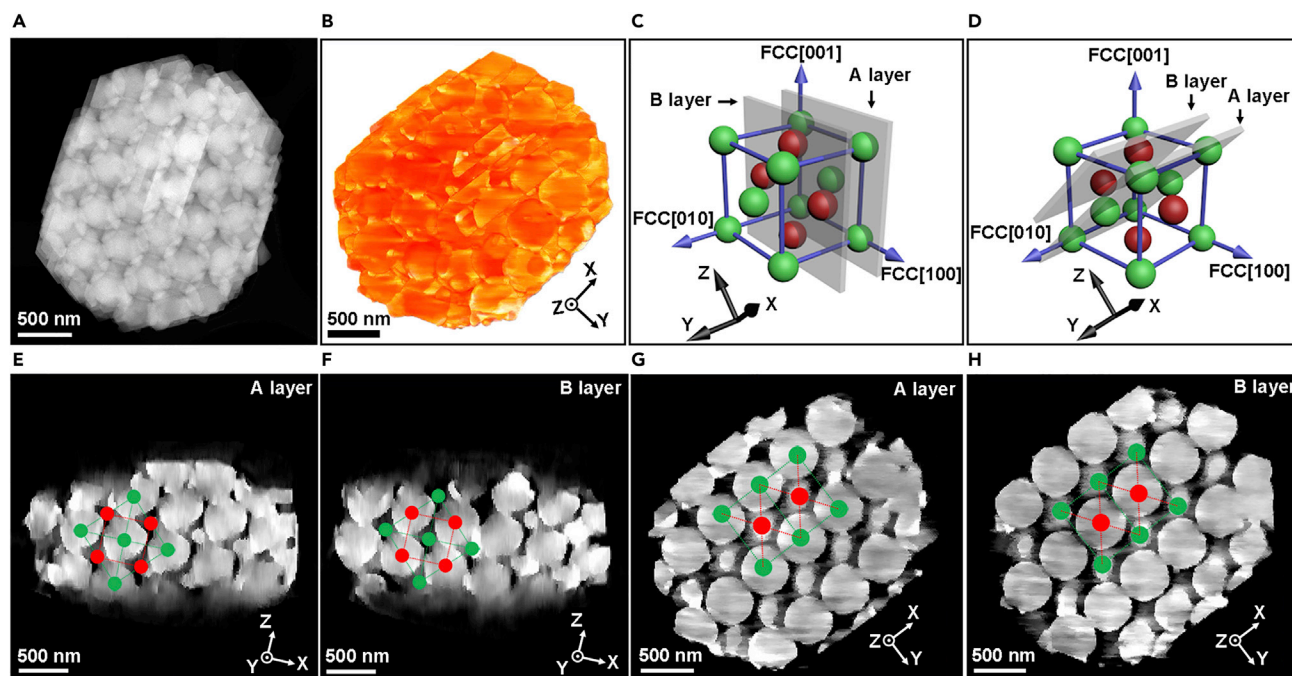


**Figure 3. STEM Tomography of OMMS-ZSM-5**

(A and B) HAADF-STEM image (A) and corresponding 3D tomographic reconstruction (B) of an individual OMMS-ZSM-5(400,30) crystal.

(C and D) Schematic illustration of the FCC unit along the y axis (C) and z axis (D).

(E and F) HAADF-STEM images of two adjacent orthoslices obtained from the 3D reconstruction: A layer (E) and B layer (F) (xz plane, perpendicular to the y axis).

(G and H) HAADF-STEM images of two adjacent orthoslices obtained from the 3D reconstruction: A layer (G) and B layer (H) (xy plane, perpendicular to the z axis).

OMMS-ZSM-5(400,30) is confirmed by  $N_2$  adsorption-desorption experiments. The steep adsorption of  $N_2$  in the  $0.6 < p/p_0 < 1.0$  region corresponds to the capillary condensation in the mesopores (Figure S8A), with the mesopore size distribution centered at 35 nm. The mesoporous surface area and total volume are  $166 \text{ m}^2 \text{ g}^{-1}$  and  $0.27 \text{ m}^3 \text{ g}^{-1}$  (Table S1), respectively. The presence of meso- and macropores in OMMS-ZSM-5(400,30) is fully confirmed by means of mercury intrusion porosimetry measurement showing (inset of Figure 2P) a narrow mesopore distribution centered at  $\sim 35$  nm, the same as the value obtained by the  $N_2$  adsorption, and a broader macroporous distribution centered at  $\sim 100$  nm. These interconnected and periodically ordered mesopores and macropores stem from the tetrahedral and octahedral voids within OMMS-ZSM-5 single crystals, respectively (Figure 1G). The presence of the highly ordered mesopores of 35 nm and macropores of 100 nm is also evidenced by the theoretical calculation and TEM and SEM observations (Figures S4 and S5), showing the consistency between the results obtained from  $N_2$  adsorption, mercury intrusion, theoretical calculations, and TEM and SEM observations. The  $^{27}\text{Al}$  magic-angle spinning (MAS) NMR spectrum (Figure S9A) indicates that aluminum atoms solely exist in the tetrahedral position ( $\delta = 55$  ppm), and no extra-framework aluminum species ( $\delta = 0$  ppm) are found. The  $^{29}\text{Si}$  MAS NMR spectrum (Figure S9D) shows that the framework primarily consists of crosslinked  $Q^4$  silica units ( $\delta = -114$  ppm,  $\text{Si}(\text{OSi})_4$ ) and  $Q^3$  silica units ( $\delta = -106$  ppm,  $\text{Si}(\text{OSi})_3(\text{OH})$  and/or  $\text{Si}(\text{O-Si})_3(\text{OAl})$ ) without  $Q^2$  units, indicative of complete condensation of the framework.

HAADF-STEM (Figure 3A) and three-dimensional (3D) electron tomographic reconstruction (Figure 3B; Video S2) of OMMS-ZSM-5(400,30) demonstrate again that

each zeolite single crystal is constructed by densely stacked and tightly interconnected small zeolite spheres of ~400 nm diameter. For a better visualization of the arrangement of the intergrown small zeolite spheres, slices along three different axes are shown in [Video S2](#). For the slices along the y axis, two neighboring layers in OMMS-ZSM-5(400,30) ([Figures 3E and 3F](#)) correspond to the (010) planes in an FCC arrangement ([Figure 3C](#)). Similarly, for the slices along the z axis, two neighboring layers in OMMS-ZSM-5(400,30) ([Figures 3G and 3H](#)) correspond to the (−101) planes in an FCC arrangement ([Figure 3D](#)). These results confirm that small zeolite spheres are densely stacked in a closely packed FCC arrangement within an individual zeolite single crystal, consistent with the inverse opal structure of the carbon template ([Figure S1](#)). It is important to note that these small uniform zeolite spheres are all tightly interconnected by the joints ([Figures 3C–3H; Video S2](#)), which are formed due to the simultaneous formation of small zeolite spheres through the windows connecting macropores of the OMMC template ([Figure S1](#)). All the above results clearly demonstrate that highly crystalline zeolite single crystals with a hierarchically porous network with fully interconnected, ordered, and multimodal porosity at macro-, meso-, and microlength scale, as in leaves, are obtained.

The diameter of the spheres in OMMS-ZSM-5 single crystals can be tuned from 200 to 600 nm by using OMMCs with different macropore sizes ([Figure S1](#)), resulting in tunable tetrahedral and octahedral voids and, thus, tunable intracrystalline mesopore and macropore sizes in each zeolite single crystal ([Figures S10–S12; Table S1](#)). The Si/Al ratio of OMMS-ZSM-5 can also easily be tuned from 30 to  $\infty$  ([Figures S13–S15](#)). The excellent mechanical, thermal, and hydrothermal stability ([Figure S16](#)) of our OMMS-ZSM-5 single crystals has been evidenced through a series of high-pressure and high-temperature treatment with and without vapor. The poor (hydro)thermal stability of the Nano-ZSM-5 ([Figure S17](#)) compared with those of zeolite single crystals with ordered intracrystalline macro-/meso-/microporous hierarchy further demonstrates the superiority of zeolite single crystals. Such high stability of zeolites under very severe conditions is of great importance for their catalytic applications.

### Catalytic Performance in Bulky-Molecule Cracking and MTO

The significant superiority of such unique hierarchical porous structure of our zeolite single crystals is first revealed in the catalytic cracking of bulky 1,3,5-TIPB ([Table S2](#)). The benchmark commercial micro-sized mesoporous ZSM-5 (C-ZSM-5) and the state-of-the-art nanosized macroporous ZSM-5 (Nano-ZSM-5) have been used as reference catalysts. The detailed adsorption-desorption and SEM characterization ([Figures S18 and S19; Table S1](#)) shows clearly that the benchmark C-ZSM-5 has mesopores at 2 nm and the state-of-the-art Nano-ZSM-5 has macropores at 51 nm. These two samples containing hierarchically multiple porosity (micro-/mesopores for the benchmark C-ZSM-5 and micro-/macropores for the state-of-the-art Nano-ZSM-5) are thus excellent references for comparison with our micro-/meso-/macroporous zeolite single crystals. The benchmark C-ZSM-5 and the state-of-the-art Nano-ZSM-5 give very low (10.65%) and medium (48.40%) conversion, respectively. In contrast, OMMS-ZSM-5(400,30), used as a representative sample, is the most active, with a conversion of 55.06%. Considering their similar Si/Al ratio (20–30) and acidities ([Table S3](#)), the improved catalytic activities in the conversion of bulky molecules over OMMS-ZSM-5(400,30) are directly related to the leaf-like open and interconnected intracrystalline hierarchically ordered micro-/meso-/macroporous architecture.

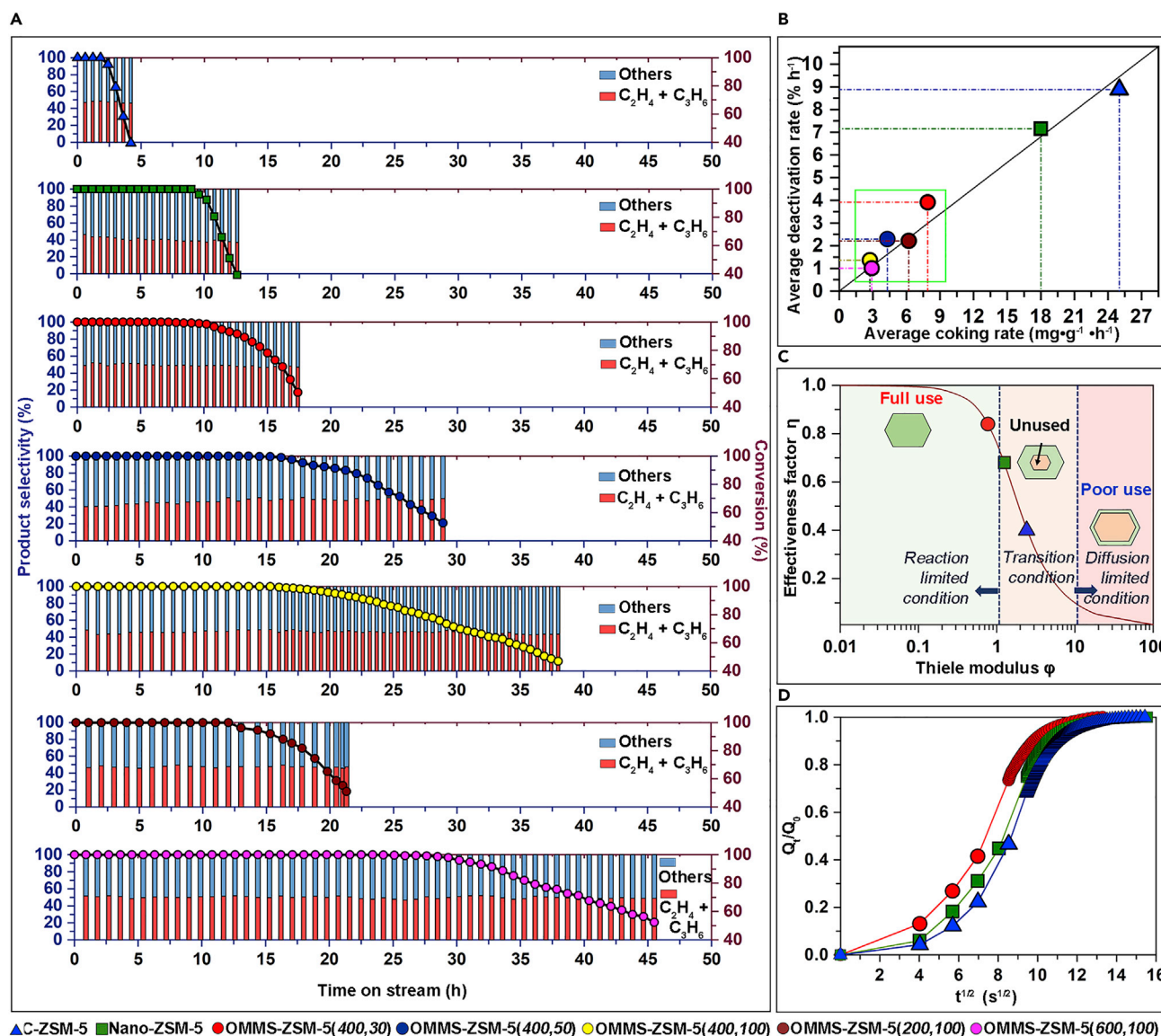


**Figure 4. Catalytic Performance, Effectiveness Factor, and Diffusion Effectiveness of OMMS-ZSM-5**

(A) Catalytic performances over various catalysts in the MTO reaction. Circles denote  $CH_3OH$  and dimethyl ether conversion, whereas bars represent product selectivities.

(B) The correlation between the average coking rate and the deactivation rate of different catalysts.

(C) Effectiveness factor  $\eta$  as a function of Thiele modulus  $\phi$  of different catalysts in the cracking of 1,3,5-triisopropylbenzene.

(D) Normalized uptake ( $Q_t/Q_0$ ) profiles of 1,3,5-trimethylbenzene over different catalysts.

The performance boost is further evidenced in the MTO process. It is well known that the delayed transport of the reactants and products in zeolite channels usually accelerates the accumulation of coke, which in turn blocks the micropores and negatively affects not only the lifetime and the zeolite utilization efficiency, but also the selectivity of the zeolite catalyst.<sup>46–49</sup> Thus, microporous zeolites are very sensitive to deactivation due to coke formation. For a better comparison, all the catalytic tests are made under harsh conditions with a high weight hourly space velocity (WHSV) of  $3.6 h^{-1}$  (see [Experimental Procedures](#)). It is clearly seen ([Figure 4A](#); [Table 1](#)) that C-ZSM-5 suffers from a rapid deactivation after only  $\sim 2.4$  h on stream, much earlier than Nano-ZSM-5 (9.0 h). The lifetime extension of OMMS-ZSM-5(400,30) is 5-

**Table 1. Catalytic Activities for MTO Reactions over Various Catalysts**

Catalyst	Si/Al <sup>a</sup> (mol mol <sup>-1</sup> )	Lifetime <sup>b</sup> (h <sup>-1</sup> )	Average Deactivation Rate <sup>c</sup> (% h <sup>-1</sup> )	Coke Amount (%)	Average Coke Rate in MTO <sup>d</sup> (mg g <sup>-1</sup> h <sup>-1</sup> )	Relative Diffusion Rate <sup>e</sup> (s <sup>1/2</sup> )
C-ZSM-5	23	2.4	25.0	3.73	8.88	0.0116
Nano-ZSM-5	21	9.0	18.0	9.01	7.15	0.0181
OMMS-ZSM-5(400,30)	30	12.5	7.90	7.06	3.92	0.0330
OMMS-ZSM-5(400,50)	50	18.5	4.31	6.62	2.29	0.0767
OMMS-ZSM-5(400,100)	100	20.4	2.73	5.15	1.36	0.0477
OMMS-ZSM-5(200,100)	100	14.1	6.20	4.72	2.21	0.0421
OMMS-ZSM-5(600,100)	100	31.0	2.91	4.59	1.01	0.0805

<sup>a</sup>Determined by the elemental analysis (inductively coupled plasma).

<sup>b</sup>The time for which the conversion of methanol exceeds 95%.

<sup>c</sup>Representing the percent loss of conversion from 95% to 50% per hour.

<sup>d</sup>Calculated by the mass loss per gram of catalyst over lifetime; the mass loss was accounted for between 300°C and 700°C.

<sup>e</sup>The slope of the fitted line in normalized uptake profile, in which  $t^{1/2}$  of the drops lower than  $2 \text{ s}^{1/2}$  (Equation 4).

and 1.4-fold longer than C-ZSM-5 and Nano-ZSM-5, respectively (Figure 4A; Table 1). The selectivity of ethylene and propylene (Figures 4A, S20, and S21) is found to be ~45% over C-ZSM-5 and from 45% to 40% over Nano-ZSM-5 with time on stream. The highest selectivity (~50%) to ethylene and propylene is observed for OMMS-ZSM-5(400,30). More importantly, such high selectivity to light olefins remains almost constant during the whole catalytic testing. The average coking rate is only  $3.92 \text{ mg g}^{-1} \text{ h}^{-1}$  for OMMS-ZSM-5(400,30), much lower than  $8.88 \text{ mg g}^{-1} \text{ h}^{-1}$  and  $7.15 \text{ mg g}^{-1} \text{ h}^{-1}$  for C-ZSM-5 and Nano-ZSM-5, respectively (Table 1). These results show not only that our OMMS-ZSM-5(400,30) sample gives the highest selectivity to ethylene and propylene in MTO reaction, but also that its average deactivation rate is 3.2- and 2.3-fold lower than that of C-ZSM-5 and Nano-ZSM-5 catalysts, respectively.

More importantly, the catalytic performances of OMMS-ZSM-5 in the MTO process can be significantly improved by varying the Si/Al ratio and, in particular, intracrystalline mesopore and macropore size. A clear correlation between the Si/Al ratio and the deactivation behavior is evidenced in Figure 4B and Table 1. A higher Si/Al molar ratio in the zeolite catalyst results in a lower deactivation rate and a reduced coke-formation rate of the catalysts, leading to a longer lifetime in the MTO reaction (Figure 4B; Table 1). The correlation between the Si/Al ratio and catalyst lifetime appears to be linear in the tested OMMS-ZSM-5s with the sphere size of 400 nm. By increasing Si/Al ratio from 30 to 100, the lifetime of OMMS-ZSM-5(400,100) (Si/Al = 100) (20.4 h) is nearly 2-fold longer than that of OMMS-ZSM-5(400,30) (Si/Al = 30). The Si/Al molar ratio of our ZSM-5 single crystals has only a minor effect on their final catalytic selectivity of ethylene and propylene, with all values staying between 45% and 50%. The interconnection and size of their intracrystalline micro-/meso-/macropores are therefore crucial factors in determining their catalytic lifetime (Figure 4B; Table 1). Among all the samples, OMMS-ZSM-5(600,100), with the largest mesopore and macropore sizes, exhibits the lowest coke-formation rate ( $1.01 \text{ mg g}^{-1} \text{ h}^{-1}$ ), being 8.9- and 7.2-fold lower than that of C-ZSM-5 and Nano-ZSM-5 catalysts, and the longest lifetime (31 h), being 13- and 3.5-fold longer than that of C-ZSM-5 and Nano-ZSM-5 catalysts, respectively. As the benchmark C-ZSM-5 and the state-of-the-art Nano-ZSM-5 contain only micro-/mesoporosity and



micro-/macroporosity, respectively, we attribute the above excellent catalytic performance to the improved diffusion behavior of the embedded larger intracrystalline pore size (Table S1) and to the completely open hierarchically interconnected and ordered micro-/meso-/macroporous structure of the ZSM-5 single crystals. As a result, the products can easily escape from the microporous channels and side reactions are significantly avoided, leading to high propylene and ethylene selectivity, a much lower coke formation and deactivation rate, and a substantial improvement in catalytic lifetime.<sup>50,51</sup> A linear correlation between deactivation rate and average coke-formation rate in MTO reaction is established among all tested ZSM-5 catalysts with different physicochemical characteristics, irrespective of their microsize, nano-size, or interconnected hierarchical structure, or even different Si/Al molar ratio (Figure 4B). This further confirms that the resistance of zeolites to deactivation is mostly correlated with the suppression of coke formation. Consequently, accelerating the transport of reactants and products is of crucial importance in designing long-lived catalysts.

### Diffusion Behavior and Catalytic Efficiency

Generally it is believed that both introducing an additional macro-/mesopore system within an individual zeolite crystal and decreasing the crystal size can improve the accessibility of reactant molecules to the active sites of the zeolites. However, our findings demonstrate that an open, interconnected, and intracrystalline hierarchically ordered micro-/meso-/macroporous structure as exists in leaves is much more favorable. To illustrate the differences between our zeolite single crystals with interconnected micro-/meso-/macroporosity and the benchmark C-ZSM-5 with micro-/mesoporosity and nanosized ZSM-5 with micro-/macroporosity in diffusion and catalytic efficiency, we performed a kinetic study over 1,3,5-TIPB cracking reaction. By the Thiele modulus analysis method (Equations 1, 2, and 3; Table S2), the utilization efficiency and effective diffusion length/rate in C-ZSM-5, Nano-ZSM-5, and OMMS-ZSM-5(400,30) are calculated. The variation of the effectiveness factor  $\eta$  related to the observed reaction rate as a function of the Thiele modulus  $\phi$ <sup>48</sup> is presented in Figure 4C, and the  $\eta$  and  $\phi$  values of studied zeolites are presented in Table S2.  $\phi$  values drawn from C-ZSM-5, Nano-ZSM-5, and OMMS-ZSM-5(400,30) are significantly different (Table S2). Assuming that the diffusivity in all MFI microporous networks is the same,<sup>34,52</sup> the obtained characteristic diffusion length  $L$  of Nano-ZSM-5 and OMMS-ZSM-5(400,30) are found to be shortened to 50% and 30%, respectively, compared with that of C-ZSM-5. The effective diffusion rate ( $D_{\text{eff}}/L^2$  derived from  $\frac{L_1}{L_2} = \frac{\phi_1}{\phi_2} \sqrt{\frac{k_2 D_{\text{eff},1}}{k_1 D_{\text{eff},2}}}$ ) of Nano-ZSM-5 is enhanced by 2-fold compared with C-ZSM-5 while that of OMMS-ZSM-5 (400,30) reaches 10- and 5-fold higher than that of C-ZSM-5 and Nano-ZSM-5, respectively, due to the effectively shortened diffusion length. The utilization efficiency  $\eta$  of C-ZSM-5 gives a generally observed value of 0.4 due to severe internal restricted diffusion because of the large size of the 1,3,5-TIPB molecule. That of Nano-ZSM-5 increases to 0.68 due to the large reduction in crystal size to nanometer scale while OMMS-ZSM-5(400,30) reaches the highest, and a high value  $\eta$  of 0.84. From Figure 4C, the OMMS-ZSM-5(400,30) is located in the full-use regime while C-ZSM-5 is in the diffusion-limited regime, showing poor utilization efficiency of C-ZSM-5 catalyst in 1,3,5-TIPB cracking reaction and explaining its low catalytic activity and short lifetime. This is in excellent agreement with the MTO reaction results. By varying mesopore and macropore size within each of our ZSM-5 single crystals, the effective diffusion rate and catalyst utilization efficiency and performance can be further improved (Table 1; Figure 4A). The continuous-flow variable-temperature hyperpolarized <sup>129</sup>Xe NMR (Figure S22) and the PFG NMR techniques (Figure S23) comprehensively

confirm the high quality and excellent accessibility of the hierarchical pore network structures, and their interconnectivity in OMMS-ZSM-5.

To further compare the differences between the diffusion behavior and the accessibility to acid sites under dynamic condition of hierarchically porous zeolite single crystals, the benchmark C-ZSM-5, and the nanosized zeolite, we performed an intelligent gravimetric analysis (IGA) on the diffusion of 1,3,5-trimethylbenzene (1,3,5-TMB) under inert conditions (Figures 4D and S24; Tables 1 and S4; Equation 4). It is believed that only a few 1,3,5-TMB molecules (kinetic diameter = 0.78 nm) can penetrate the micropores (= 0.55 nm) while most of them will only be adsorbed onto the external surface of microporous zeolites. In comparison, the interparticle macropores of Nano-ZSM-5 and the ordered macro-/mesoporous networks of OMMS-ZSM-5(400,30) offer sufficient space for more 1,3,5-TMB molecules. The relative diffusion rate of OMMS-ZSM-5(400,30) sample, which is calculated by linear fits of the normalized uptake profile ( $Q_t/Q_0$ ), is 1.8- and 2.8-fold higher than those in Nano-ZSM-5 and C-ZSM-5. The adsorption amount of 1,3,5-TMB at dynamic conditions at different diffusion time was measured for OMMS-ZSM-5(400,30), OMMS-ZSM-5(600,100), C-ZSM-5, and Nano-ZSM-5 (Figure S23; Table S4). It is clearly seen that at dynamic condition, OMMS-ZSM-5 zeolite single crystals have much higher accessibility to acid sites than C-ZSM-5 and Nano-ZSM-5. This observation is directly linked to the excellent connectivity between micropores and meso-/macropores of OMMS-ZSM-5 zeolite single crystals. The highest adsorption amounts of 1,3,5-TMB and the highest diffusivity observed for OMMS-ZSM-5 (600, 100) explain its best catalytic performance. The results obtained by the laser hyperpolarized  $^{129}\text{Xe}$  NMR, the PFG  $^{129}\text{Xe}$  NMR, kinetic study of 1,3,5-TIPB cracking reaction, and diffusion and dynamic accessibility of 1,3,5-TMB by IGA, all in excellent consistency, explain the excellent catalytic performance of OMMS-ZSM-5 zeolite single crystal. The highly ordered hierarchically micro-/meso-/macroporous structure of ZSM-5 single crystals is thus a decisive factor in improving the mass transfer property. By varying mesopore and macropore size within each of our ZSM-5 single crystals, the relative diffusion rate of OMMS-ZSM-5(600,100) with the largest mesopore and macropore size is found to be 7- and 4.5-fold higher than that of C-ZSM-5 and Nano-ZSM-5. The above results show that the highly ordered and interconnected hierarchically macro-/mesoporous structure inside our zeolite single crystal is much more effective than macroporous nanocrystals. Such unique hierarchically porous architecture can maximize the intracrystalline diffusion rate of reactants and products by reducing effective diffusion length, leading to much higher zeolite utilization efficiency, a significant reduction in coking and deactivation rates, and improved catalyst lifetime.<sup>53,54</sup>

## Conclusions

ZSM-5 single crystals with a highly interconnected and ordered intracrystalline macro-/mesoporous system and variable Si/Al ratios and tunable mesopore and macropore size have been successfully synthesized by a bottom-up confined crystallization process. The hierarchical porous system in the single crystals results in a significantly improved diffusion performance for various reactants compared with the benchmark commercial micro-sized micro-/mesoporous and micro-/macroporous nanosized zeolite counterparts, leading to excellent catalytic performance in bulky-molecule reaction and MTO process. Using OMMS-ZSM-5(400, 30) as an example, not only is the catalytic activity much higher in bulky-molecule cracking reaction, the effective diffusion rate of molecules reaches 10- and 5-fold higher than that of benchmark commercial micro-/mesoporous C-ZSM-5 and the state-of-the-art micro-/macroporous Nano-ZSM-5, respectively. Its utilization efficiency in the

1,3,5-TIPB cracking reaction can reach a very high value of 0.84, which is double that of C-ZSM-5 catalyst and 20% higher than that of Nano-ZSM-5 catalyst. The average coking rate in MTO reaction is 2.2- and 1.7-fold lower than that of C-ZSM-5 and Nano-ZSM-5, respectively. Most importantly, the catalytic performances of our zeolite single crystals can be significantly improved by varying the Si/Al ratio and, in particular, by adjusting the intracrystalline mesopore and macropore size. The relative diffusion rate of OMMS-ZSM-5(600,100), with the largest mesopore and macropore size (Table 1), can reach even 7- and 4.5-fold higher than that of C-ZSM-5 and Nano-ZSM-5, respectively, and its average coking rate in MTO reaction can attain 8.9- and 7.2-fold lower than that of C-ZSM-5 and C-ZSM-5, respectively. Compared with C-ZSM-5 and Nano-ZSM-5 catalysts, the lifetime of this sample can be extended 13- and 3.5-fold longer, respectively.

Our synthesis route to zeolite single crystals is not only simple and readily upscalable but also highly versatile, and has already been extended to the successful synthesis of other zeolite structures and zeotype materials, including Beta, TS-1, MOR, Y, and SAPO-34. The utilization of such zeolite single crystals with excellent properties to a large series of industrial catalytic reactions can lead to the design of innovative and intensified reactors and processes with highly enhanced efficiency, high catalytic activity, selectivity, and lifetime, and minimum energy, time, and raw-material consumption. The zeolite single-crystal reactor concept can be exploited. Most importantly, our synthesis strategy can be extended to fabricate single-crystalline solids of any chemical compositions such as transition metal oxides (e.g., TiO<sub>2</sub>, ZnO), phosphate compounds, silicate compounds, and perovskites. The key parameters in the construction of hierarchical porous structure within each single crystal by our innovative confined crystallization method are the control of the water content in the dried precursor gel and the occupancy rate and crystallization rate of dried precursor gel confined in the hierarchical porous template. The utilization of such single-crystalline solids in a various reactions and procedures can lead to a revolution in industrial processes.

## EXPERIMENTAL PROCEDURES

### Resource Availability

#### Lead Contact

Further information and requests for resources and reagents should be directed to and will be fulfilled by the lead contact, Bao-Lian Su ([bao-lian.su@unamur.be](mailto:bao-lian.su@unamur.be)).

#### Materials Availability

OMMS-ZSM-5s generated in this study will be made available on request, but we may require a payment and/or a completed Materials Transfer Agreement if there is potential for commercial application.

#### Data and Code Availability

The data supporting the findings of this study are available in the article and [Supplemental Information](#), or from the lead contact upon request.

### Hierarchical Zeolite Single-Crystal Preparation

#### Synthesis of Uniform Polystyrene Spheres with Tunable Diameter

Uniform PS spheres with a diameter of 220 nm were synthesized by emulsion polymerization. Sodium laurylsulfonate (emulsifying agent, 0.6 g) was dissolved in 360 g of deionized H<sub>2</sub>O followed by addition of 47 g of styrene. After adding 0.54 g of potassium persulfate, the reaction was performed at 75°C for 4.5 h under an argon atmosphere. PS spheres with monodispersed sizes of about 220 nm were obtained.

Uniform PS spheres with a diameter of 420 nm were synthesized by soap-free polymerization. Styrene (47 g) was added in 400 g of deionized H<sub>2</sub>O followed by addition of 0.43 g of potassium persulfate. The reaction was performed at 80°C for 5 h under an argon atmosphere. PS spheres with monodispersed sizes of about 420 nm were obtained.

Uniform PS spheres with a diameter of 620 nm were synthesized by soap-free polymerization. Styrene (49 g) was added in 430 g of deionized H<sub>2</sub>O followed by addition of 0.51 g of potassium persulfate. The reaction was performed at 70°C for 11 h under an argon atmosphere. PS spheres with monodispersed sizes of about 620 nm were obtained.

#### *Synthesis of Hierarchically Ordered Macro-/Mesoporous Carbon with Tunable Diameter*

In a typical procedure, the mass composition of the initial reaction mixtures is 100PS/15SiO<sub>2</sub>/15C<sub>12</sub>H<sub>22</sub>O<sub>11</sub>/1.5H<sub>2</sub>SO<sub>4</sub>. PS spheres (as-synthesized) were first blended with silica sol (Ludox AS-40 colloidal silica) under magnetic stirring for 1 h. The obtained colloidal suspension was mixed with sucrose at room temperature for 10 min. Sulfuric acid was then slowly added under stirring for another 10 min to obtain a stable dispersion. The as-prepared dispersion was directly dried in an oven at 110°C for 6 h, then at 160°C for 6 h, followed by heating to 700°C with a rate of 2°C min<sup>-1</sup> under pure nitrogen flow (1 L min<sup>-1</sup>). The temperature was kept at 700°C for 4 h to decompose the polymer spheres and carbonize sucrose. The obtained carbon/silica composite was cooled in pure nitrogen and immersed in a 10 wt % hydrofluoric acid aqueous solution to remove silica, followed by washing with deionized water and drying at 60°C to yield OMMC. The size of the macropores in OMMC can be tuned by varying the size of the corresponding PS spheres (220 nm, 420 nm, 620 nm). OMMC templates with a macropore size of ~200 nm (OMMC-200), ~400 nm (OMMC-400), and ~600 nm (OMMC-600) were obtained, respectively.

#### *Synthesis of Ordered and Interconnected Hierarchically Macro-/Meso-/Microporous ZSM-5 Single Crystals with Tunable Meso-/Macroporosity and Tunable Si/Al Molar Ratio*

A bottom-up confined crystallization process was used for the confined synthesis of hierarchical ordered macro-mesoporous ZSM-5 single crystals within the OMMC templates. In a typical synthesis, OMMC with different macropore size was impregnated with an excess solution of tetrapropylammonium hydroxide (TPAOH), tetraethyl orthosilicate, aluminum isopropoxide, and water. The molar composition of the initial reaction mixture is 0.36TPAOH/SiO<sub>2</sub>/xAl<sub>2</sub>O<sub>3</sub>/19.2 H<sub>2</sub>O (x = 0.067, 0.040, 0.020). After slow evaporation of water from the mixture of the precursors confined in OMMC template at room temperature, the mixture was transferred to a Teflon-lined stainless-steel autoclave equipped with a porous metallic network suspended at the middle of the autoclave for holding the mixture. Sufficient water was placed at the bottom of autoclave to produce saturated steam. The SAC process was performed at 180°C for 10 h. Thereafter, the samples were taken out of the autoclave and washed by filtration with abundant deionized water. Finally, the product was dried at 60°C and further calcined at 550°C for 7 h to remove the carbon template. The as-synthesized samples are denoted by OMMS-ZSM-5(x,y) (OMMS represents ordered macro-mesoporous single-crystalline), where x and y represent the macropore size of OMMC templates and Si/Al molar ratio. In this work, OMMS-ZSM-5s with controllable mesopore and macropore size and tunable Si/Al ratio were obtained: OMMS-ZSM-5(200,100), OMMS-ZSM-5(400,100), OMMS-ZSM-5(600,100), OMMS-ZSM-5(400,30), and OMMS-ZSM-5(400,50).



C-ZSM-5 and Nano-ZSM-5 from Fuyu New Materials Technology were used as reference samples with Si/Al ratios of 23 and 21, respectively.

### Catalyst Characterization

XRD patterns were recorded on a Bruker D8 Advance diffractometer using CuK $\alpha$  monochromatized radiation ( $\lambda = 1.5418 \text{ \AA}$ ). The measurements were taken at 45 kV and 40 mA in a continuous mode and a  $2\theta$  range from  $5^\circ$  to  $60^\circ$  with a step increase of  $0.02^\circ$ .

SEM images were obtained on a Hitachi S4800 field-emission scanning electron microscope operated at 5 kV and 10  $\mu\text{A}$ . TEM, HRTEM, SAED, and HAADF-STEM studies were performed on a Thermo Fisher Titan Themis 60-300 "cubed" microscope fitted with double aberration-correctors for both TEM and STEM, operated at 120 kV. 3D reconstruction was performed through an Astra Tomography Toolbox.

The chemical composition of the samples was determined by inductively coupled plasma optical emission spectroscopy using a PerkinElmer Optima 4300DV. The wavelength range was 165–782 nm and resolution was 0.006 nm (at 200 nm).

Ar and N<sub>2</sub> adsorption-desorption isotherms were recorded using a Micromeritics ASAP 2020 gas sorptiometer after the samples were degassed at 300°C under vacuum for 12 h. The micropore surface area was determined from Ar adsorption isotherm using the t-plot method. By using the model based on non-local density functional theory, micropore volume and micropore size were derived from the adsorption branches of Ar isotherms with relative pressure  $p/p_0$  of  $<0.01$ . The mesopore surface area was determined from N<sub>2</sub> adsorption using the Brunauer-Emmett-Teller method. Using the Barret-Joyner-Halenda model, mesopore volume and mesopore size were determined by the adsorption branches of N<sub>2</sub> isotherms. Total pore volumes were estimated from the adsorbed amount at a relative pressure  $p/p_0$  of 0.99.

Mercury intrusion porosimetry was performed with a Micromeritics Autopore IV 9500 operated in the pressure range from vacuum to 207 MPa. Samples were degassed *in situ* prior to measurement. The pore size distribution was determined by application of the Washburn equation. The macropore volume was determined by the volume of Hg intruded into pores of  $>50 \text{ nm}$  diameter.

The NMR spectra were recorded at room temperature using a Varian VNMRS spectrometer operating at 9.4 T ( $^{27}\text{Al}$  freq. = 79.46 MHz;  $^{29}\text{Si}$  freq. = 79.46 MHz). The probe used was a Varian/Chemagnetics HX 4-mm CP/MAS. The samples were packed in a standard 4-mm rotor and spun at 10 kHz. The number of transients range between  $\sim 200$  and 11,000 for the  $^{29}\text{Si}$  spectra, and between 2,000 and 3,500 for the  $^{27}\text{Al}$  spectra. For the  $^{27}\text{Al}$  spectra, the parameters were: spectral width  $\sim 104 \text{ kHz}$ , relaxation delay 100 ms, excitation pulse 3  $\mu\text{s}$ , acquisition time 5 ms. For  $^{29}\text{Si}$  spectra, the parameters were: spectral width  $\sim 104 \text{ kHz}$ , relaxation delay 6 ms, excitation pulse 3  $\mu\text{s}$ , acquisition time 5 ms.

Laser hyperpolarized  $^{129}\text{Xe}$  NMR experiments were carried out at 110.6 MHz on a Varian Infinity-plus 400 spectrometer using a 7.5-mm probe. Before each experiment, samples (60–80 mesh) were dehydrated at 673 K under vacuum ( $<10^{-5} \text{ torr}$ ) for 24 h. The optical polarization of xenon was achieved with a homemade apparatus with the optical pumping cell in the fringe field of the spectrometer magnet and a 60-W diode laser array (Coherent FAP-System). A flow of gas mixture

(1% Xe/1% N<sub>2</sub>/98% He) was delivered at the rate of 100–150 mL min<sup>−1</sup> to the sample in the detection region via plastic tubing. Variable-temperature NMR measurements were performed in the range of 153–273 K. All one-dimensional spectra were acquired with 3.0-μs  $\pi/2$  pulse, 100–200 scans, and 2-s recycle delay. The chemical shifts were referenced to the signal of xenon gas. Although the line of the xenon gas is temperature dependent, generally chemical shifts vary no more than 1 ppm in the temperature range of the experiments.

Prior to PFG NMR diffusion measurements, the sample was dehydrated on a vacuum system at 673 K for 16 h. The samples were then transferred into the NMR tube with pressure valve in a glovebox. After degassing overnight at 393 K, Xe was quantitatively introduced into the NMR tube on a homemade uptake apparatus. After Xe adsorption, the tube was sealed and equilibrated at room temperature. The loading of adsorbed xenon was calculated by the ideal gas equation. All data were acquired at equilibrium condition. <sup>129</sup>Xe PFG NMR experiments were conducted on a 600-MHz Bruker Avance III spectrometer equipped with a 5-mm Diff50 diffusion probe delivering a maximum gradient of 1800 G cm<sup>−1</sup> in the z direction. A bipolar-gradient stimulated echo sequence (STEAP, 13-interval pulse sequence) was applied in diffusion measurements to eliminate distortions of the PFG NMR results by internal magnetic field inhomogeneities (i.e., internal magnetic field gradients) induced by susceptibility variations in heterogeneous samples.

The acidity of the samples was determined by NH<sub>3</sub> temperature-programmed desorption using a Micromeritics ASAP 2920. For measurement, 50 mg of sample powder was introduced into a quartz reactor and degassed under vacuum at 550°C. After cooling to room temperature, NH<sub>3</sub> gas was adsorbed for 1 h. This was followed by evacuation at 120°C to remove free and weakly adsorbed NH<sub>3</sub>. The desorption profile was then measured with evacuation at the temperature gradient of 10°C min<sup>−1</sup>, using a thermal conductivity detector.

### Catalytic Stability Test

For the mechanical stability test, the samples were pressed under pressure at 5 MPa, 10 MPa, and 15 MPa. The resultant samples were characterized by SEM and XRD.

For the thermal stability test, the samples were treated in a muffle furnace at two different temperatures, 800°C and 1,000°C, for 1 h. The resultant samples were characterized by SEM, XRD, and Ar gas adsorption.

For the hydrothermal stability test, the samples were pressed into molds and placed into a high-temperature hydrothermal aging tube under N<sub>2</sub> flow. Once the temperature reached 780°C, N<sub>2</sub> flow was shut down. The samples were then treated in saturated steam at 780°C for 2 h. The resultant samples were characterized by XRD and Ar gas adsorption.

### Catalytic Activity Test

Before the catalytic activity evaluation, all the samples were converted into H<sup>+</sup> form. As a typical run, the sample was ion-exchanged with NH<sub>4</sub>NO<sub>3</sub> (0.6 M) aqueous solution at 80°C for 3 h, followed by calcination at 550°C for 6 h. This procedure was repeated three times. The MTO reaction was performed in a stainless-steel microcatalytic reactor. The catalyst sample (0.19 g) was first diluted with 1.81 g of quartz sand into a well-distributed mixture and placed in a microcatalytic reactor, preheated at 500°C for 1 h under N<sub>2</sub> flow (50 mL min<sup>−1</sup>) beforehand. After settling the temperature at 480°C, methanol was uniformly pumped into a preheated device

(180°C) to transform into vapor phase and then mixed with N<sub>2</sub> flow (90 mL min<sup>-1</sup>) into a homogeneous phase. For a better and quicker comparison, the tests were under conducted harsh conditions using a high WHSV of methanol feedstock. The WHSV was set at 3.6 h<sup>-1</sup>. The products were collected (time interval 0.6 h<sup>-1</sup>) and analyzed by an on-line gas chromatograph (Agilent 6820) equipped with a flame ionization detector. For the conversion calculations, dimethyl ether was considered as a reactant rather than a product.

### Kinetic Evaluation

Bulky 1,3,5-TIPB cracking reaction was employed to quantitatively determine effective diffusivity and reactivity of different MFI zeolite catalysts. The reaction was taken in a specially made stainless-steel catalytic microreactor. Catalyst sample (0.12 g) was dispersed in 4.68 g of quartz sand. The mixture was then preheated at 500°C for 1 h under N<sub>2</sub> flow before reaction. 1,3,5-TIPB was uniformly pumped into the preheated device to transform the liquid into vapor, which was then mixed with N<sub>2</sub> as the carrier gas. The contact time was adjusted by changing the flow rate of the gas mixture. The catalytic activities of the zeolite samples were evaluated at different temperatures. The products were analyzed by an on-line gas chromatograph (Agilent 6820) equipped with a flame ionization detector. Before the catalytic test, the elimination of external diffusion was confirmed by establishing the conversion-contact time curves over different amounts of catalysts.

The rate constants of different zeolites in the 1,3,5-TIPB cracking reaction at different temperatures and the reaction activation energy with/without diffusion limit (i.e., apparent/intrinsic activation energy,  $E_{app,a}/E_{int,a}$ ) in zeolite catalysts have been calculated by fitting with Arrhenius equation. Thiele modulus  $\phi$  is defined as Equation 1 and can be obtained by Equation 2. Effectiveness factor  $\eta$  was calculated by Equation 3 for zeolite with geometry of flat plate (thickness  $2L$ ).

$$\phi = \sqrt{\frac{r_{intrinsic}}{r_{diffusion}}} = L \sqrt{\frac{K}{D_{A,eff}}}, \quad (\text{Equation 1})$$

where  $\phi$  is the Thiele modulus,  $r_{intrinsic}$  is the maximum reaction rate,  $r_{diffusion}$  is the maximum diffusion rate,  $L$  is the distance from the center of the catalyst pellet to the surface,  $K$  is the reaction rate constant, and  $D_{A,eff}$  is the effective diffusivity in the zeolite pores.

$$\frac{E_{app,a}}{E_{int,a}} = \frac{1}{2} + \phi \frac{1 - \tanh h^2 \phi}{2 \tanh h \phi}, \quad (\text{Equation 2})$$

where  $E_{app,a}$  is the reaction activation energy with diffusion limit (i.e., apparent activation energy),  $E_{int,a}$  is the reaction activation energy without diffusion limit (i.e., intrinsic activation energy), and  $\phi$  is the Thiele modulus.

$$\eta = \frac{\tanh h \phi}{\phi}, \quad (\text{Equation 3})$$

where  $\eta$  is the effectiveness factor and  $\phi$  is the Thiele modulus.

### Diffusion and Dynamic Accessibility Test

1,3,5-TMB diffusion measurement in ZSM-5 zeolites was performed using a computer-controlled intelligent gravimetric analyzer (Hiden Analytical, Warrington, UK). An ultrahigh vacuum system was employed by which adsorption isotherms and corresponding kinetics can be accurately acquired. A sensitive microbalance (resolution of 0.2  $\mu$ g) was mounted in an enclosure with fitted thermostat to remove thermal coefficients of the weighing system and thus provide high stability and

accuracy. The zeolite sample ( $100 \pm 1$  mg) was degassed under vacuum ( $<10^{-5}$  Pa) at  $450^{\circ}\text{C}$  for 10 h prior to the adsorption measurement. The system temperature was then set at  $50^{\circ}\text{C}$ , regulated within  $0.1^{\circ}\text{C}$  by a water bath. The relative pressure was rapidly raised to 0.099 and then kept constant during the tests. For each step, the amount of adsorbate introduced in the system was kept small enough to keep the adsorption process isothermal. The weight increase of sorbents was automatically measured by a microbalance and continuously recorded as a function of time under the settled gas vapor pressure.

Diffusion coefficient  $D$  was obtained based on Fick's Law. Equation 4 gives the fitting formula of diffusion coefficient  $D$  for zeolite with geometry of flat plate.

$$\frac{Q_t - Q_0}{Q_{\infty} - Q_0} = 1 - \sum_{n=0}^{\infty} \frac{8}{[(2n+1)\pi]^2} \exp\left[\frac{-D(2n+1)^2\pi^2 t}{h^2}\right] \approx \frac{8}{\sqrt{\pi^2}} \left(\frac{D}{h^2}\right)^{1/2} \sqrt{t} \quad (\text{where } t \text{ is small}),$$

(Equation 4)

where  $Q_0$  is the initial adsorbed quantity,  $Q_t$  is the intermediate adsorbed quantity,  $Q_{\infty}$  is the equilibrium adsorbed quantity,  $n$  is the natural numbers,  $D$  is the diffusion coefficient for zeolite with geometry of flat plate (thickness  $h = 2L$ ),  $t$  is the adsorbed time, and  $h$  is the thickness of zeolite.

## SUPPLEMENTAL INFORMATION

Supplemental Information can be found online at <https://doi.org/10.1016/j.matt.2020.07.016>.

## ACKNOWLEDGMENTS

This work is supported by Program for Changjiang Scholars and Innovative Research Team in University (IRT\_15R52) of the Chinese Ministry of Education. B.-L.S. acknowledges the Chinese Ministry of Education for a "Changjiang Chaire Professor" position and a Clare Hall Life Membership, University of Cambridge. L.-H.C. acknowledges Hubei Provincial Department of Education for the "Chutian Scholar" program. Z.-Y.H. and G.V.T. acknowledge the support from the Center for Materials Research and Analysis and the State Key Laboratory of Silicate Materials for Architectures at Wuhan University of Technology. This work is also financially supported by NSFC-21671155, NSFC-U1663225, Major programs of technical innovation in Hubei (2018AAA012), and Hubei Provincial Natural Science Foundation (2018CFA054), Fundamental Research Funds for the Central Universities (WUT: 2018III039GX, 2019III012GX, 2020III002GX). We thank the 111 Project (grant no. B20002) from the Ministry of Science and Technology and the Ministry of Education of China, and the project "DepollutAir" of Interreg V France-Wallonie-Vlaanderen for supporting this work.

## AUTHOR CONTRIBUTIONS

L.-H.C. and B.-L.S. conceived the project. L.-H.C., Z.-K.X., G.V.T., and B.-L.S. supervised the study. M.-H.S. designed and performed experiments, characterized samples, analyzed data, and wrote the draft of the manuscript. J.Z. performed the catalysis reactions, analyzed the catalysis data, and performed kinetic evaluation. Z.-Y.H. and S.T. performed TEM and tomography analysis. L.-Y.L. and Y.-D.W. performed the diffusion test and analyzed the diffusion data. T.H. provided advice for the writing of the manuscript. L.-H.C. wrote the manuscript. L.-H.C., G.V.T., Z.-K.X., T.H., and B.-L.S. revised the manuscript, and B.-L.S. finalized the manuscript.



## DECLARATION OF INTERESTS

The authors declare no competing interests.

Received: January 18, 2020

Revised: June 3, 2020

Accepted: July 8, 2020

Published: August 12, 2020

## REFERENCES

- Gallego, E.M., Portilla, M.T., Paris, C., León-Escamilla, A., Boronat, M., Moliner, M., and Corma, A. (2017). "Ab initio" synthesis of zeolites for preestablished catalytic reactions. *Science* 355, 1051–1054.
- Jiao, F., Li, J., Pan, X., Xiao, J., Li, H., Ma, H., Wei, M., Pan, Y., Zhou, Z., Li, M., et al. (2016). Selective conversion of syngas to light olefins. *Science* 351, 1065–1068.
- Slater, A.G., and Cooper, A.I. (2015). Functional design of new porous materials. *Science* 348, aaa8075.
- Snyder, B.E.R., Vanelderen, P., Bols, M.L., Hallaert, S.D., Böttger, L.H., Ungur, L., Pierloot, K., Schoonheydt, R.A., Sels, B.F., and Solomon, E.I. (2016). The active site of low-temperature methane hydroxylation in iron-containing zeolites. *Nature* 536, 317–321.
- Schneider, D., Mehlhorn, D., Zeigermann, P., Kärger, J., and Valiullin, R. (2016). Transport properties of hierarchical micro-mesoporous materials. *Chem. Soc. Rev.* 45, 3439–3467.
- Schwieger, W., Machoke, A.G., Weissenberger, T., Inayat, A., Selvam, T., Klumpp, M., and Inayat, A. (2016). Hierarchy concepts: classification and preparation strategies for zeolite containing materials with hierarchical porosity. *Chem. Soc. Rev.* 45, 3353–3376.
- Lopez-Orozco, S., Inayat, A., Schwab, A., Selvam, T., and Schwieger, W. (2011). Zeolitic materials with hierarchical porous structures. *Adv. Mater.* 23, 2602–2615.
- Hartmann, M., Machoke, A.G., and Schwieger, W. (2016). Catalytic test reactions for the evaluation of hierarchical zeolites. *Chem. Soc. Rev.* 45, 3313–3330.
- Valtchev, V., Majano, G., Mintova, S., and Pérez-Ramírez, J. (2013). Tailored crystalline microporous materials by post-synthesis modification. *Chem. Soc. Rev.* 42, 263–290.
- Sun, M.-H., Huang, S.-Z., Chen, L.-H., Li, Y., Yang, X.-Y., Yuan, Z.-Y., and Su, B.-L. (2016). Applications of hierarchically structured porous materials from energy storage and conversion, catalysis, photocatalysis, adsorption, separation, and sensing to biomedicine. *Chem. Soc. Rev.* 45, 3479–3563.
- Zheng, X., Shen, G., Wang, C., Li, Y., Dunphy, D., Hasan, T., Brinker, C.J., and Su, B.-L. (2017). Bio-inspired murray materials for mass transfer and activity. *Nat. Commun.* 8, 14921.
- Roth, W.J., Nachtigall, P., Morris, R.E., Wheatley, P.S., Seymour, V.R., Ashbrook, S.E., Chlubná, P., Grajciar, L., Polojž, M., Zukal, A., et al. (2013). A family of zeolites with controlled pore size prepared using a top-down method. *Nat. Chem.* 5, 628–633.
- Mitchell, S., Michels, N.-L., Kunze, K., and Pérez-Ramírez, J. (2012). Visualization of hierarchically structured zeolite bodies from macro to nano length scales. *Nat. Chem.* 4, 825–831.
- De Jong, K.P., Zečević, J., Friedrich, H., De Jongh, P.E., Bulut, M., Van Donk, S., Kennogne, R., Finiels, A., Hulea, V., and Fajula, F. (2010). Zeolite Y crystals with trimodal porosity as ideal hydrocracking catalysts. *Angew. Chem. Int. Ed.* 49, 10074–10078.
- Qin, Z., Cychosz, K.A., Melinte, G., El Siblani, H., Gilson, J.-P., Thommes, M., Fernandez, C., Mintova, S., Ersen, O., and Valtchev, V. (2017). Opening the cages of faujasite-type zeolite. *J. Am. Chem. Soc.* 139, 17273–17276.
- Jacobsen, C.J.H., Madsen, C., Houzvicka, J., Schmidt, I., and Carlsson, A. (2000). Mesoporous zeolite single crystals. *J. Am. Chem. Soc.* 122, 7116–7117.
- Fan, W., Snyder, M.A., Kumar, S., Lee, P.-S., Yoo, W.C., McCormick, A.V., Penn, R.L., Stein, A., and Tsapatsis, M. (2008). Hierarchical nanofabrication of microporous crystals with ordered mesoporosity. *Nat. Mater.* 7, 984–991.
- Lee, P.-S., Zhang, X., Stoeger, J.A., Malek, A., Fan, W., Kumar, S., Yoo, W.C., Al Hashimi, S., Penn, R.L., Stein, A., et al. (2011). Sub-40 nm zeolite suspensions via disassembly of three-dimensionally ordered mesoporous-imprinted silicalite-1. *J. Am. Chem. Soc.* 133, 493–502.
- Liu, D., Bhan, A., Tsapatsis, M., and Al Hashimi, S. (2011). Catalytic behavior of Brønsted acid sites in MWW and MFI zeolites with dual meso- and microporosity. *ACS Catal.* 1, 7–17.
- Chen, H., Wydra, J., Zhang, X., Lee, P.-S., Wang, Z., Fan, W., and Tsapatsis, M. (2011). Hydrothermal synthesis of zeolites with three-dimensionally ordered mesoporous-imprinted structure. *J. Am. Chem. Soc.* 133, 12390–12393.
- Machoke, A.G., Beltran, A.M., Inayat, A., Winter, B., Weissenberger, T., Kruse, N., Güttel, R., Spiecker, E., and Schwieger, W. (2015). Micro/macroporous system: MFI-type zeolite crystals with embedded macropores. *Adv. Mater.* 27, 1066–1070.
- Weissenberger, T., Reiprich, B., Machoke, A.G.F., Klühspies, K., Bauer, J., Dotzel, R., Casci, J.L., and Schwieger, W. (2019). Hierarchical MFI type zeolites with intracrystalline macropores: the effect of the macropore size on the deactivation behaviour in the MTO reaction. *Catal. Sci. Technol.* 9, 3259–3269.
- Weissenberger, T., Machoke, A.G., Bauer, J., Dotzel, R., Casci, J., Hartmann, M., and Schwieger, W. (2020). Hierarchical ZSM-5 catalysts: the effect of different intracrystalline pore dimensions on catalyst deactivation behaviour in the MTO reaction. *ChemCatChem* 12, 2461–2468.
- Weissenberger, T., Leonhardt, R., Zubiri, B.A., Pitínová-Šteková, M., Sheppard, T.L., Reiprich, B., Bauer, J., Dotzel, R., Kahnt, M., Schropp, A., et al. (2019). Synthesis and characterisation of hierarchically structured titanium silicalite-1 zeolites with large intracrystalline macropores. *Chem. Eur. J.* 25, 14430–14440.
- Na, K., Jo, C., Kim, J., Cho, K., Jung, J., Seo, Y., Messinger, R.J., Chmelka, B.F., and Ryoo, R. (2011). Directing zeolite structures into hierarchically nanoporous architectures. *Science* 333, 328–332.
- Xu, D., Ma, Y., Jing, Z., Han, L., Singh, B., Feng, J., Shen, X., Cao, F., Oleynikov, P., Sun, H., et al. (2014).  $\pi$ - $\pi$  interaction of aromatic groups in amphiphilic molecules directing for single-crystalline mesostructured zeolite nanosheets. *Nat. Commun.* 5, 4262.
- Liu, F., Willhammar, T., Wang, L., Zhu, L., Sun, Q., Meng, X., Carrillo-Cabrera, W., Zou, X., and Xiao, F.-S. (2012). ZSM-5 zeolite single crystals with b-axis-aligned mesoporous channels as an efficient catalyst for conversion of bulky organic molecules. *J. Am. Chem. Soc.* 134, 4557–4560.
- Zhu, J., Zhu, Y., Zhu, L., Rigutto, M., van der Made, A., Yang, C., Pan, S., Wang, L., Zhu, L., Jin, Y., et al. (2014). Highly mesoporous single-crystalline zeolite Beta synthesized using a nonsurfactant cationic polymer as a dual-function template. *J. Am. Chem. Soc.* 136, 2503–2510.
- Pérez-Ramírez, J., Christensen, C.H., Egeblad, K., Christensen, C.H., and Groen, J.C. (2008). Hierarchical zeolites: enhanced utilisation of microporous crystals in catalysis by advances in materials design. *Chem. Soc. Rev.* 37, 2530–2542.
- Cychosz, K.A., Guillet-Nicolas, R., García-Martínez, J., and Thommes, M. (2017). Recent advances in the textural characterization of hierarchically structured nanoporous materials. *Chem. Soc. Rev.* 46, 389–414.
- Mitchell, S., Pinar, A.B., Kenvin, J., Crivelli, P., Karger, J., and Pérez-Ramírez, J. (2015). Structural analysis of hierarchically organized zeolites. *Nat. Commun.* 6, 8633.

32. Groen, J.C., Peffer, L.A.A., and Pérez-Ramírez, J. (2003). Pore size determination in modified micro- and mesoporous materials. Pitfalls and limitations in gas adsorption data analysis. *Micropor. Mesopor. Mater.* **60**, 1–17.
33. Michels, N.-L., Mitchell, S., Milina, M., Kunze, K., Krumeich, F., Marone, F., Erdmann, M., Marti, N., and Pérez-Ramírez, J. (2012). Hierarchically structured zeolite bodies: assembling micro-, meso-, and macroporosity levels in complex materials with enhanced properties. *Adv. Funct. Mater.* **22**, 2509–2518.
34. Gueudré, L., Milina, M., Mitchell, S., and Pérez-Ramírez, J. (2014). Superior mass transfer properties of technical zeolite bodies with hierarchical porosity. *Adv. Funct. Mater.* **24**, 209–219.
35. Thibault-Starzyk, F., Stan, I., Abelló, S., Bonilla, A., Thomas, K., Fernandez, C., Gilson, J.-P., and Pérez-Ramírez, J. (2009). Quantification of enhanced acid site accessibility in hierarchical zeolites – the accessibility index. *J. Catal.* **264**, 11–14.
36. Zubiaga, A., Warringham, R., Boltz, M., Cooke, D., Crivelli, P., Gidley, D., Pérez-Ramírez, J., and Mitchell, S. (2016). The assessment of pore connectivity in hierarchical zeolites using positron annihilation lifetime spectroscopy: instrumental and morphological aspects. *Phys. Chem. Chem. Phys.* **18**, 9211–9219.
37. Kenyon, J., Mitchell, S., Sterling, M., Warringham, R., Keller, T.C., Crivelli, P., Jagiello, J., and Pérez-Ramírez, J. (2016). Quantifying the complex pore architecture of hierarchical faujasite zeolites and the impact on diffusion. *Adv. Funct. Mater.* **26**, 5621–5630.
38. Liu, Y., Zhang, W., Liu, Z., Xu, S., Wang, Y., Xie, Z., Han, X., and Bao, X. (2008). Direct observation of the mesopores in ZSM-5 zeolites with hierarchical porous structures by laser-hyperpolarized  $^{129}\text{Xe}$  NMR. *J. Phys. Chem. C* **112**, 15375–15381.
39. Chen, L.-H., Xu, S.-T., Li, X.-Y., Tian, G., Li, Y., Rooke, J.C., Zhu, G.-S., Qiu, S.-L., Wei, Y.-X., Yang, X.-Y., et al. (2012). Multimodal Zr-silicalite-1 zeolite nanocrystal aggregates with interconnected hierarchically micro-meso-macroporous architecture and enhanced mass transport property. *J. Colloid Interface Sci.* **377**, 368–374.
40. Galarneau, A., Guenneau, F., Gedeon, A., Mereib, D., Rodriguez, J., Fajula, F., and Coasne, B. (2016). Probing interconnectivity in hierarchical microporous/mesoporous materials using adsorption and nuclear magnetic resonance diffusion. *J. Phys. Chem. C* **120**, 1562–1569.
41. Kärger, J., and Valiullin, R. (2013). Mass transfer in mesoporous materials: the benefit of microscopic diffusion measurement. *Chem. Soc. Rev.* **42**, 4172–4197.
42. Milina, M., Mitchell, S., Cooke, D., Crivelli, P., and Pérez-Ramírez, J. (2015). Impact of pore connectivity on the design of long-lived zeolite catalysts. *Angew. Chem. Int. Ed.* **54**, 1591–1594.
43. Zhang, S., Chen, L., Zhou, S., Zhao, D., and Wu, L. (2010). Facile synthesis of hierarchically ordered porous carbon via *in situ* self-assembly of colloidal polymer and silica spheres and its use as a catalyst support. *Chem. Mater.* **22**, 3433–3440.
44. Li, F., Wang, Z., and Stein, A. (2007). Shaping mesoporous silica nanoparticles by disassembly of hierarchically porous structures. *Angew. Chem. Int. Ed.* **46**, 1885–1888.
45. Kokotailo, G.T., Lawton, S.L., Olson, D.H., and Meier, W.M. (1978). Structure of synthetic zeolite ZSM-5. *Nature* **272**, 437–438.
46. Weckhuysen, B.M., and Yu, J. (2015). Recent advances in zeolite chemistry and catalysis. *Chem. Soc. Rev.* **44**, 7022–7024.
47. Milina, M., Mitchell, S., Crivelli, P., Cooke, D., and Pérez-Ramírez, J. (2014). Mesopore quality determines the lifetime of hierarchically structured zeolite catalysts. *Nat. Commun.* **5**, 3922.
48. Losch, P., Pinar, A.B., Willinger, M.G., Soukup, K., Chavan, S., Vincent, B., Pale, P., and Louis, B. (2017). H-ZSM-5 zeolite model crystals: structure-diffusion-activity relationship in methanol-to-olefins catalysis. *J. Catal.* **345**, 11–23.
49. Olsbye, U., Svelle, S., Bjørgen, M., Beato, P., Janssens, T.V., Joensen, F., Bordiga, S., and Lillerud, K.P. (2012). Conversion of methanol to hydrocarbons: how zeolite cavity and pore size controls product selectivity. *Angew. Chem. Int. Ed.* **51**, 5810–5831.
50. Bibby, D.M., Howe, R.F., and McLellan, G.D. (1992). Coke formation in high-silica zeolites. *Appl. Catal. A Gen.* **93**, 1–34.
51. Bibby, D.M., Milestone, N.B., Patterson, J.E., and Aldridge, L.P. (1986). Coke formation in zeolite ZSM-5. *J. Catal.* **97**, 493–502.
52. Groen, J.C., Zhu, W.D., Brouwer, S., Huynink, S.J., Kapteijn, F., Moulijn, J.A., and Pérez-Ramírez, J. (2007). Direct demonstration of enhanced diffusion in mesoporous ZSM-5 zeolite obtained via controlled desilication. *J. Am. Chem. Soc.* **129**, 355–360.
53. Zhao, L., Shen, B., Gao, J., and Xu, C. (2008). Investigation on the mechanism of diffusion in mesopore structured ZSM-5 and improved heavy oil conversion. *J. Catal.* **258**, 228–234.
54. Baur, R., and Krishna, R. (2005). The effectiveness factor for zeolite catalysed reactions. *Catal. Today* **105**, 173–179.